ELSEVIER

Physica D 151 (2001) 83–98

PHYSICA D

www.elsevier.com/locate/physd

Fourier–Bessel analysis of patterns in a circular domain

Shuguang Guan [a], C.-H. Lai [a], G.W. Wei [b,*]

[a] *Department of Physics, National University of Singapore, Singapore 117543, Singapore*
[b] *Department of Computational Science, National University of Singapore, Singapore 117543, Singapore*

Received 29 February 2000; received in revised form 28 October 2000; accepted 5 January 2001
Communicated by A.C. Newell

Abstract

This paper explores the use of the Fourier–Bessel analysis for characterizing patterns in a circular domain. A set of stable patterns is found to be well-characterized by the Fourier–Bessel functions. Most patterns are dominated by a principal Fourier–Bessel mode $[n, m]$ which has the largest Fourier–Bessel decomposition amplitude when the control parameter R is close to a corresponding non-trivial root ($\rho_{n,m}$) of the Bessel function. Moreover, when the control parameter is chosen to be close to two or more roots of the Bessel function, the corresponding principal Fourier–Bessel modes compete to dominate the morphology of the patterns.

PACS: 47.54.+r; 05.70.Np; 05.65.+b; 05.10.−a; 02.30.Nw

Keywords: Fourier–Bessel analysis; Circular domain; Cahn–Hilliard equation

1. Introduction

The continued miniaturization of electronic devices leads to a new realm of nanostructures, such as functional ceramics, functional films, supermolecular electronic packages, magnetic storage devices and polymeric drug delivery systems that exhibit novel electronic, superamolecular and magnetic properties. Quantum well and quantum dot devices are already widespread. Recently, much effort has been devoted to the design of quantum wires and quantum dots with specified properties. The nanotechnology of the future will require the creation and control of nanostructures at desirable shape, desirable size and desirable arrangement of functional groups. A general strategy for controlled self-assembly of spherical and cylindrical supermolecules has been recently reported [1]. What is most relevant to our work is the boundary effects in the design and control of nanostructures. It is well understood that the boundary of a nano-device plays an extremely important role in the global properties of the device. Moreover, the self-organization process of nano-device formation can be controlled by a confining boundary. It has been reported that boundary-confined polymerizations can lead to thin films which possess dramatically different properties from those of ordinary polymers [2].

There are different schools of thinking for the theoretical description of nanoscale devices and formation of nanoscale patterns. The ideal approach is based on the quantum mechanical first principle, which, in fact, can be used for the estimation of certain statistical

* Corresponding author. Tel.: +65-874-6589; fax: +65-774-6756.
E-mail address: cscweigw@nus.edu.sg (G.W. Wei).

0167-2789/01/$ – see front matter
PII: S0167-2789(01)00223-8

properties. However, for the dynamics of pattern formation, the required computations are formidable for the commonly available computer resources at present. In particular, pattern formation involves mass (density), momentum, and energy transport, which is far beyond the computational power of the foreseeable future. Statistical treatment in terms of density operators, such as the BBGKY theory (derived from the first principle), provides a conceptual basis for visualizing the dynamical process of pattern formation. However, the more involved nonlinear integrodifferential equations in terms of the phase space variables are still impossible to solve at present. In contrast, phenomenological theories are generally suitable for a qualitative description [3–5]. One of the most commonly used theoretical model is the Cahn–Hilliard equation [6,5,8,20], which is similar to the Kuramoto–Sivashinsky equation [7]. In its dimensionless form, the dynamical evolution of a conserved scalar order parameter describing the phase separation and pattern formation of a binary system (A + B) is given by

$$\frac{\partial \Psi}{\partial t} = \frac{1}{2}\nabla^2(-\nabla^2\Psi - \Psi + \Psi^3), \tag{1}$$

where $\Psi(\mathbf{r}, t)$ $(-1 \leq \Psi(\mathbf{r}, t) \leq 1)$ is the conserved scalar order parameter. Usually it is chosen to be the difference between local densities of the components A and B.

In the previous work, we carried out a theoretical study of the boundary-controlled nanoscale pattern formation, using the Cahn–Hilliard equation as a mathematical model [9]. A circular geometry was chosen as the computational domain. The objective was to simulate the experiments conducted over spheres and cylinders [1]. A discrete singular convolution (DSC) algorithm [10] was utilized for the numerical integration. Extensive high-precision simulations generated a new class of patterns resembling molecular self-assembly.

The purpose of this paper is to analyze patterns generated in the circular domain. Conventional methods for pattern analysis is often based on the Fourier transform. In particular, the (Fourier) power spectrum is useful for describing energy distribution and the density of states of physical systems in R^n. However, in the circular domain, a natural basis is the Fourier–Bessel functions [18]. A complementary approach for pattern characterization is the wavelet analysis [11–15]. Recently, wavelet analysis has been used to analyze fractals and their associated dynamics. Moreover, wavelet packets are found to be useful for local characterization of turbulence and pattern recognition. In the field of pattern formation, due to the multiscale nature of patterns, wavelet transforms are regarded as "the bridge between theory and experiment" [3]. It not only allows us to extract physical information from experimental and computed patterns, but also provides us a convenient method to detect and locate pattern defects. In this study, we will focus on the use of Fourier–Bessel analysis for characterizing the stable patterns. Quantitative wavelet analysis and characterization of the spatio-temporal patterns will be presented elsewhere.

This paper is organized as follows. Section 2 is devoted to a brief description of numerical experiments and results of boundary-controlled patterns. Typical stable patterns are given as the background material for pattern characterization. Symmetry analysis is performed for the stable patterns. Fourier–Bessel analysis is conducted in Section 3. For the Cahn–Hilliard equation in the circular domain, the Fourier–Bessel decomposition not only provides a natural means for "eigenmode" analysis, but also releases dynamical information, such as modal selection and competition. This paper ends with a conclusion.

2. Patterns of ordered states

2.1. Numerical aspects

In a circular domain, it is necessary to carry out the integration of the Cahn–Hilliard equation (1) in the polar coordinates (r, θ), so that the O(2) symmetry is preserved. The involved biharmonic operator

$$\nabla^4 = \partial_{rrrr} + 2r^{-1}\partial_{rrr} - r^{-2}\partial_{rr} + r^{-3}\partial_r + 2r^{-2}\partial_{rr\theta\theta} - 2r^{-3}\partial_{r\theta\theta} + 4r^{-4}\partial_{\theta\theta} + r^{-4}\partial_{\theta\theta\theta\theta}, \tag{2}$$

generates artificial singularities up to the fourth order at the origin. Moreover, nonlinear terms may lead to

additional complexity in the phase space. Therefore, it is very challenging to integrate the Cahn–Hilliard equation in the circular domain. We overcome these numerical difficulties by utilizing a newly developed DSC algorithm [10]. The DSC approach has both controlled accuracy for maintaining integration stability and the flexibility for handling complex boundary and geometry [10,16]. It has been successfully used in the integration of the sine-Gordon equation when the initial values are chosen to be close to the most excitable homoclinic orbit [17].

The standard implicit Crank–Nicolson scheme is used for time discretization. The nonlinear terms are linearized by using a Newton-like technique. Coupled collocation equations are solved at each time step by a standard direct method. For all simulations, we choose 32 and 64 grid points in the r and θ directions, respectively. The DSC regularization parameters [10] are set as $\sigma_q/\Delta_q = 3.8\,(q = r, \theta)$ in both directions. The DSC bandwidth parameters are set to 30 in both dimensions. The radius (R) of the circular domain is used as the control parameter to regulate the pattern morphology. A given random field, generated by small amplitude noise (about 10^{-2}) inside the circular domain, is used as the initial values for all computations. Motivated by the underlying physics, we impose the Dirichlet boundary condition ($\Psi(\mathbf{r}, t) = 0$) at the edge of the circular domain. Ordered state patterns are generated by integrating Eq. (1) at a set of selected control parameters, R, ranging from 1 to 13. At each given radius, we integrate Eq. (1) up to 1000 time units, and some particular runs are integrated up to 2000 time units to attain stable patterns. In order to achieve the accuracy of spectral method level over the circular domain, all the computations were extremely expensive and time consuming in terms of computer resources.

2.2. Symmetry analysis

Fig. 1 shows the 0–255 gray-scale plots of typical patterns obtained from the numerical experiments. The basic morphology of these patterns is concentric rings of cells. Each cell can be regarded as an single-phase domain of either component A or B, formed through microphase separations. Notably, there are two interesting symmetric aspects in the observed patterns. The first is due to the conservation of order parameter

$$\iint \Psi(r, \theta, t) r \, \mathrm{d}\theta \, \mathrm{d}r = 0 \quad \forall t > 0. \tag{3}$$

Therefore, the phase separation can only occur as phase polarization with respect to the (r, θ) plane. Moreover, if Ψ is an ordered state of the system, $-\Psi$ is also a possible ordered state of the system which has the symmetric distribution of order parameter field as that of Ψ. For example, the spatial distribution of the pattern in Fig. 2(a) is a "mirror image" of the pattern shown in Fig. 1(t), i.e., the distribution of order parameter fields of these two patterns are symmetric. In fact, these two patterns correspond to the same control parameter R. Statistically, they should have equal probability to appear if the time integration is sufficiently long.

The other symmetric aspect involves geometric symmetry of the ordered state patterns. First, we note the existence of symmetric center (I) in all patterns plotted in Fig. 1. There are also rotational symmetries (C_m) classified by m values in the gray-scale plots shown in Fig. 1. For example, as shown in Fig. 1(c), (l) and (s), $m = 3$ implies a 3-fold symmetry. Obviously the combination of symmetries of the first type (C_m) and the second type (I) leads to another symmetry of the second type (σ_v). Therefore, patterns in Fig. 1 are of C_{mv} type. Further analysis in Section 3 indicates that they predominantly consist of certain Fourier–Bessel modes. For multi-ring patterns, the number of cells in different rings are usually the same, partially due to the C_{mv} symmetry. However, in some rare cases the number of cells in different rings could be different. For instance, Fig. 8(c) depicts a pattern which has two rings of cells. Unlike those patterns shown in Fig. 1, it has a single cell in the inner ring and 10 cells in the outer ring. Nevertheless, in both situations, the spatial distribution of the cells is interlacing, i.e., the signs of the order parameter of any two neighboring cells are opposite.

3. Fourier–Bessel analysis

3.1. Theoretical background

Like the use of the Fourier analysis on the rectangular domain, Fourier–Bessel analysis [18] is a powerful analysis tool in the circular domain. To illustrate the uniqueness of the Fourier–Bessel analysis for the present characterization, let us consider the linearized stationary Cahn–Hilliard equation

$$\nabla^2(\nabla^2 + 1)\tilde{\Psi} = 0. \tag{4}$$

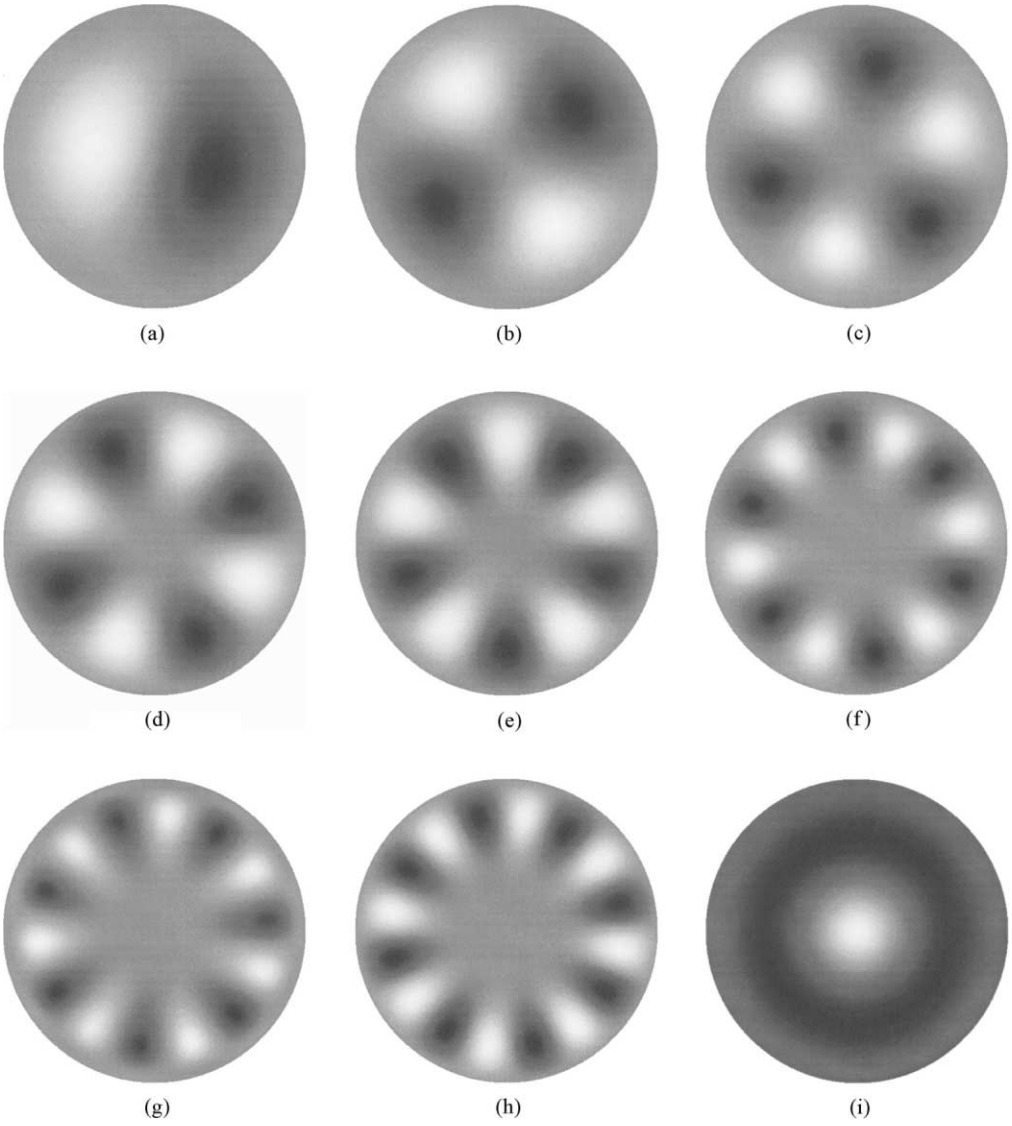

Fig. 1. 0–255 gray-scale plots of typical ordered state patterns and the initial values: (a) [1,1] ($t = 1000$); (b) [1,2] ($t = 1000$); (c) [1,3] ($t = 1240$); (d) [1,4] ($t = 1000$); (e) [1,5] ($t = 900$); (f) [1,6] ($t = 1000$); (g) [1,7] ($t = 740$); (h) [1,8] ($t = 1000$); (i) [2,0] ($t = 580$); (j) [2,1] ($t = 850$); (k) [2,2] ($t = 1000$); (l) [2,3] ($t = 1000$); (m) [2,4] ($t = 990$); (n) [2,5] ($t = 990$); (o) [2,6] ($t = 1000$); (p) [3,0] ($t = 760$); (q) [3,1] ($t = 740$); (r) [3,2] ($t = 1000$); (s) [3,3] ($t = 1000$); (t) [4,0] ($t = 700$); (u) the initial values. The corresponding control parameters are listed in Table 2.

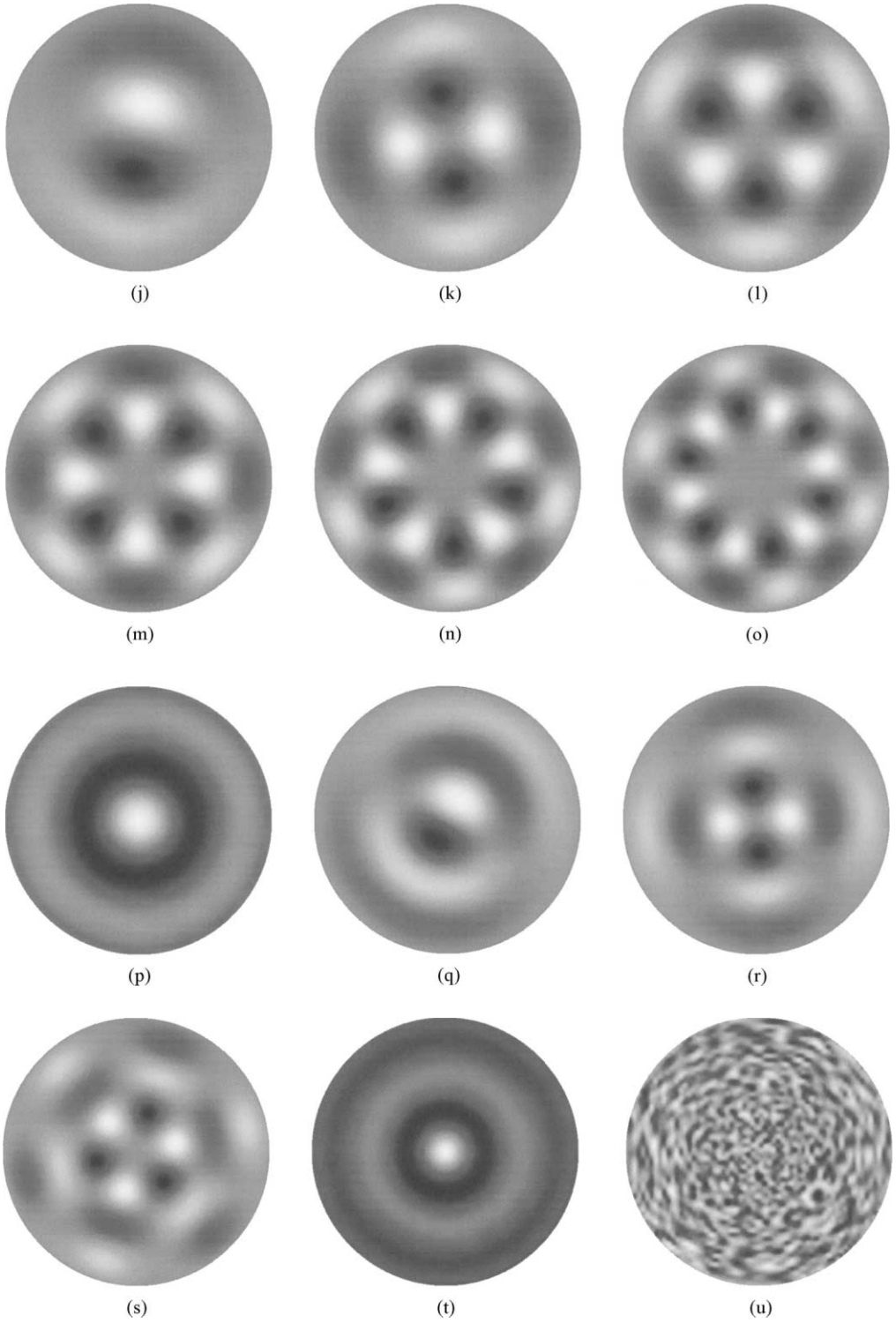

Fig. 1. (*Continued*).

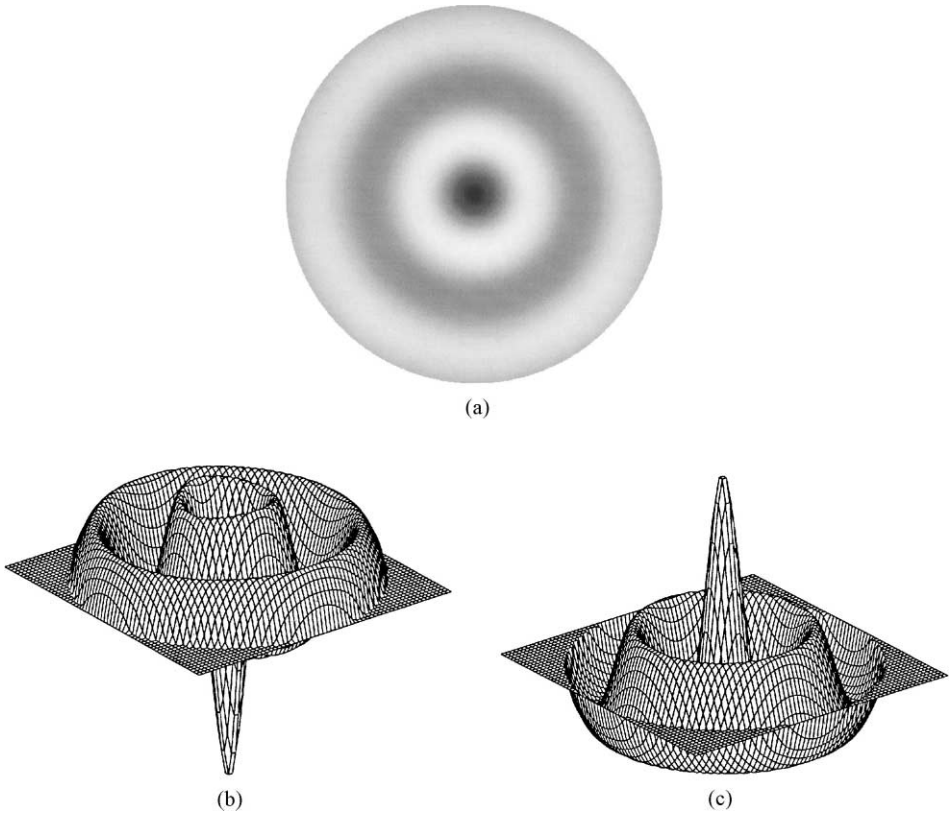

Fig. 2. (a) 0–255 gray-scale plots; (b) mesh plots of the pattern at $R = 11$, $t = 730$; (c) mesh plot corresponding to the pattern shown in Fig. 1(t).

Eq. (4) can be factorized as

$$\nabla^2\tilde{\Psi} = 0, \tag{5}$$

$$(\nabla^2 + 1)\tilde{\Psi} = 0. \tag{6}$$

Eqs. (5) and (6) are the Laplace equation and Helmholtz equation, respectively. In polar coordinates, by separation of variables $\tilde{\Psi}(r,\theta) = \Theta(\theta)B(r)$, both equations can be decomposed into

$$\frac{\mathrm{d}^2\Theta}{\mathrm{d}\theta^2} + m^2\Theta = 0, \tag{7}$$

and the Bessel equation

$$r^2\frac{\mathrm{d}^2B}{\mathrm{d}r^2} + r\frac{\mathrm{d}B}{\mathrm{d}r} + (r^2 - m^2)B = 0. \tag{8}$$

Solution to Eqs. (7) and (8) are $\mathrm{e}^{\mathrm{i}m\theta}$ and the Bessel functions, respectively. Hence, a general solution to Eq. (6) can be expressed as

$$\tilde{\Psi}(r,\theta) = \sum_{m=0}^{\infty}[A_m J_m(r) + B_m N_m(r)]\,\mathrm{e}^{\mathrm{i}m\theta}, \quad m = 0, 1, \ldots, \tag{9}$$

where $J_m(r)$ and $N_m(r)$ are the Bessel functions of the first and second kinds, respectively. Since the circular domain includes the origin, in order to avoid singularity at the origin, B_m must be set to zero. Thus the solution to Eq. (6) is

$$\tilde{\Psi}(r,\theta) = \sum_{m=0}^{\infty}A_m J_m(r)\,\mathrm{e}^{\mathrm{i}m\theta}, \quad m = 0, 1, \ldots, \tag{10}$$

i.e., the linearized stationary Cahn–Hilliard equation has the solutions of the Bessel functions of the first kind. In addition, a careful observation of the typical patterns in Fig. 1 reveals that they resemble the truncated Fourier–Bessel functions to a given radius in the circular domain. The above analysis suggests that for the full Cahn–Hilliard equation, stable solutions can be expressed as a Fourier–Bessel series

$$\Psi(r,\theta) = \sum_{n,m} Z_{n,m}\Phi_{n,m}(r,\theta) + \text{c.c.}, \tag{11}$$

where $\Phi_{n,m}(r,\theta)$, $[\Phi_{n,m}(r,\theta) = J_m(\rho_{n,m}r/R)\,\mathrm{e}^{\mathrm{i}m\theta}$ $(m \geq 0,\, n > 0)]$, is a Fourier–Bessel mode characterized by $[n,m]$, and c.c. denotes the complex conjugate. $J_m(\rho_{n,m}r/R)$ are the mth Bessel function of the first kind [19] and $\rho_{n,m}$ is its nth non-trivial root. Here, $Z_{n,m}$ are the complex coefficients except for $Z_{n,0}$, the latter is real. The orthonormality and completeness of the functions $\Phi_{n,m}(r,\theta)$ provide

$$Z_{n,m} = \frac{1}{\pi R^2 J_{m+1}^2(\rho_{n,m})} \times \int_0^{2\pi}\int_0^R \Psi(r,\theta)\bar{\Phi}_{n,m}(r,\theta) r\,\mathrm{d}\theta\,\mathrm{d}r, \quad m > 0, \tag{12}$$

while the coefficients $Z_{n,0}$ take half of the value given by the above formula when m equal to zero. Here the bar denotes the complex conjugate. Eq. (11) is used for characterizing stable patterns in the circular domain.

3.2. Modal decomposition

Since the linearized Cahn–Hilliard equation has the Bessel function as a solution, it is expected that the full solution to the Cahn–Hilliard equation would be proportional to the Fourier–Bessel functions. This is indeed the case. Each of the patterns in Fig. 1 actually resembles a Fourier–Bessel mode. However, due to the nonlinearity of Cahn–Hilliard equation and the Dirichlet boundary condition used in the computations, the possibility of pure Fourier–Bessel modes to be the solutions of our model is generally ruled out. Therefore, a quantitative analysis is required for the detailed composition of each pattern. This can be done by computing the Fourier–Bessel decomposition (expansion) coefficients $Z_{n,m}$ for each pattern plotted in Fig. 1.

Fig. 3 plots the decomposition amplitudes $|Z_{n,m}|$ of the pattern in Fig. 1(c) corresponding to the largest 20 Fourier–Bessel modes. It is found that most of the amplitudes are very small (below 10^{-2}) except that there are a few Fourier–Bessel modes whose decomposition amplitudes are significantly large. Furthermore, there is a dominant Fourier–Bessel mode whose Fourier–Bessel decomposition amplitude is much larger than the second largest amplitude and other amplitudes. It is this dominant mode that determines the morphology of the pattern. In Table 1, the three largest Fourier–Bessel decomposition amplitudes are listed for all patterns shown in Fig. 1 except for Fig. 1(u). On an average, the largest amplitude is about 0.8, while the second largest amplitude is usually below 0.1. We describe this dominant Fourier–Bessel mode as the principal Fourier–Bessel mode, which has the largest contribution to the pattern. In Fig. 1, we have classified the typical patterns according to their principal Fourier–Bessel modes in terms of their "quantum number", $[n,m]$.

It is found that the morphology of the pattern is mainly determined by the principal Fourier–Bessel mode, whereas the contributions from the non-principal Fourier–Bessel modes can slightly change the cells' shape. Fig. 4(a)–(c) depicts three patterns which are observed at the same control parameter $R = 12$. Fourier–Bessel decomposition shows that the principal Fourier–Bessel mode of these three patterns is [3, 3] and two important non-principal Fourier–Bessel modes are [2, 3] and [4, 3]. The picture of the pure Fourier–Bessel mode [3, 3] is given in Fig. 4(d). A comparison of these three patterns with the pure Fourier–Bessel mode shows that the morphology of patterns in Fig. 4(a)–(c) basically resemble that of the pure Fourier–Bessel mode [3, 3], while the outer cells in Fig. 4(b) and the middle ring in Fig. 4(c) are slightly modified. Fourier–Bessel decomposition shows that the corresponding Fourier–Bessel decomposition amplitudes of the principal Fourier–Bessel mode in these three patterns are 0.705, 0.691 and 0.676, respectively. This implies that the pure Fourier–Bessel

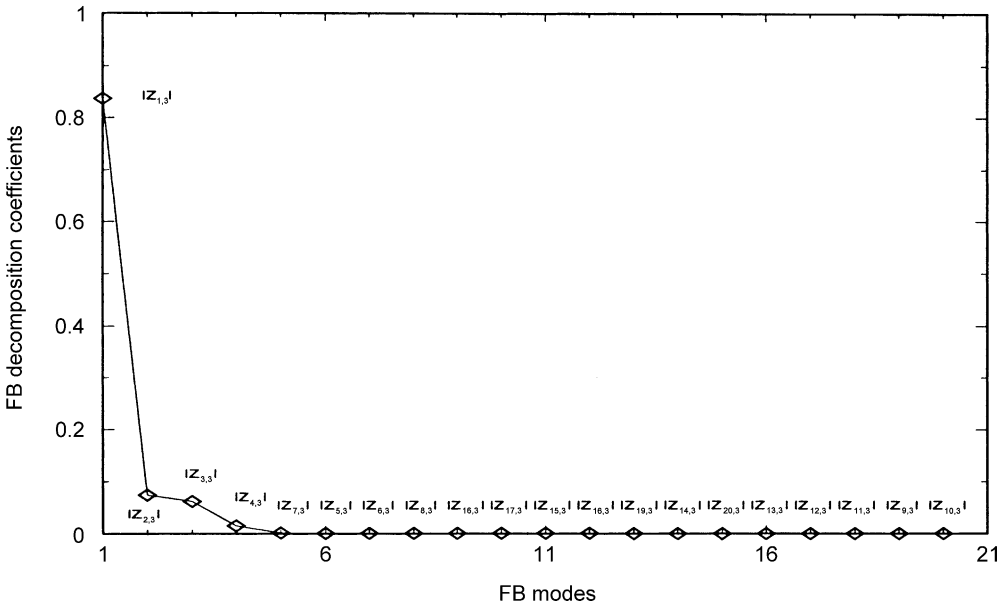

Fig. 3. Fourier–Bessel decomposition of the pattern shown in Fig. 1(c). The 20 largest Fourier–Bessel decomposition amplitudes are sorted in the decreasing order. The first four largest amplitudes are $|Z_{1,3}| = 0.837$, $|Z_{2,3}| = 0.0746$, $|Z_{3,3}| = 0.0623$ and $|Z_{4,3}| = 0.0155$, respectively. The others are all below 0.01.

Table 1
The first three largest Fourier–Bessel decomposition amplitudes for the patterns shown in Fig. 1

	First	Second	Third
(a)	$\|Z_{1,1}\| = 0.776$	$\|Z_{2,1}\| = 0.117$	$\|Z_{3,1}\| = 0.0324$
(b)	$\|Z_{1,2}\| = 0.853$	$\|Z_{2,2}\| = 0.0769$	$\|Z_{3,2}\| = 0.0262$
(c)	$\|Z_{1,3}\| = 0.837$	$\|Z_{2,3}\| = 0.0746$	$\|Z_{3,3}\| = 0.0624$
(d)	$\|Z_{1,4}\| = 0.893$	$\|Z_{2,4}\| = 0.0807$	$\|Z_{3,4}\| = 0.0102$
(e)	$\|Z_{1,5}\| = 0.762$	$\|Z_{2,5}\| = 0.0895$	$\|Z_{3,5}\| = 0.0519$
(f)	$\|Z_{1,6}\| = 0.791$	$\|Z_{3,6}\| = 0.0919$	$\|Z_{2,6}\| = 0.0475$
(g)	$\|Z_{1,7}\| = 0.848$	$\|Z_{2,7}\| = 0.0417$	$\|Z_{3,7}\| = 0.0258$
(h)	$\|Z_{1,8}\| = 0.906$	$\|Z_{2,8}\| = 0.0438$	$\|Z_{3,1}\| = 0.0170$
(i)	$\|Z_{2,0}\| = 0.496$	$\|Z_{1,0}\| = 0.128$	$\|Z_{3,0}\| = 0.106$
(j)	$\|Z_{2,1}\| = 0.719$	$\|Z_{3,1}\| = 0.101$	$\|Z_{4,1}\| = 0.0625$
(k)	$\|Z_{2,2}\| = 0.744$	$\|Z_{3,2}\| = 0.0926$	$\|Z_{4,2}\| = 0.0634$
(l)	$\|Z_{2,3}\| = 0.775$	$\|Z_{3,3}\| = 0.0845$	$\|Z_{4,3}\| = 0.0608$
(m)	$\|Z_{2,4}\| = 0.809$	$\|Z_{3,4}\| = 0.0592$	$\|Z_{4,4}\| = 0.0583$
(n)	$\|Z_{2,5}\| = 0.831$	$\|Z_{3,5}\| = 0.0479$	$\|Z_{4,5}\| = 0.0464$
(o)	$\|Z_{2,6}\| = 0.705$	$\|Z_{4,6}\| = 0.0971$	$\|Z_{3,6}\| = 0.0492$
(p)	$\|Z_{3,0}\| = 0.361$	$\|Z_{1,0}\| = 0.0972$	$\|Z_{4,2}\| = 0.0949$
(q)	$\|Z_{3,1}\| = 0.816$	$\|Z_{4,1}\| = 0.0614$	$\|Z_{2,1}\| = 0.0377$
(r)	$\|Z_{3,2}\| = 0.773$	$\|Z_{1,2}\| = 0.0622$	$\|Z_{2,2}\| = 0.0564$
(s)	$\|Z_{3,3}\| = 0.705$	$\|Z_{4,3}\| = 0.151$	$\|Z_{2,3}\| = 0.0924$
(t)	$\|Z_{4,0}\| = 0.513$	$\|Z_{2,0}\| = 0.0969$	$\|Z_{3,0}\| = 0.0794$

mode contributes approximately the same to these three patterns. We attribute the minor difference of the morphology of the patterns to the existence of many non-principal Fourier–Bessel modes. Another interesting example is the pattern in Fig. 1(p). Although the Fourier–Bessel decomposition amplitude of the principal Fourier–Bessel mode is 0.361, which is the smallest among all the amplitudes of principal Fourier–Bessel modes listed in Table 1, the morphology of the pattern is predominantly determined by the principal Fourier–Bessel mode $[3, 0]$, which is shown in Fig. 5(a). In Fig. 5(b), we show the contour plot for the difference between the computed pattern Fig. 1(p) and the pure Fourier–Bessel mode $[3, 0]$. It is found that the contribution from the non-principal Fourier–Bessel modes only makes the edge of the outer ring slightly rough. Apart from this minor change, non-principal modes contribute very little to the basic morphology of the pattern.

It is noted that the amplitudes of principal Fourier–Bessel modes $[n, 0]$ ($n = 2, 3, 4$) are relatively smaller compared to those of the other

patterns. The Fourier–Bessel decomposition amplitudes for the principal Fourier–Bessel modes [2, 0], [3, 0] and [4, 0] are $|Z_{2,0}| = 0.496$, $|Z_{3,0}| = 0.361$ and $|Z_{4,0}| = 0.513$, respectively. Strictly speaking, these patterns are complicated super-positions of many Fourier–Bessel modes. For example, there are 19 Fourier–Bessel decomposition amplitudes that are greater than 0.01 for the pattern shown in Fig. 1(p). Fig. 6 depicts these amplitudes in their decreasing order. It is also noted that the Fourier–Bessel decomposition amplitudes of all non-principal Fourier–Bessel modes are very small (less than 0.1). This phenomenon is due to the fact that the Dirichlet boundary condition leads to a boundary stress at the pattern edge, which is not compatible to the principal Fourier–Bessel modes of $[n, 0]$ type.

3.3. Modal competition

The system tends to stabilize at a principal Fourier–Bessel mode $[n, m]$ when the control parameter R is close to the corresponding non-trivial

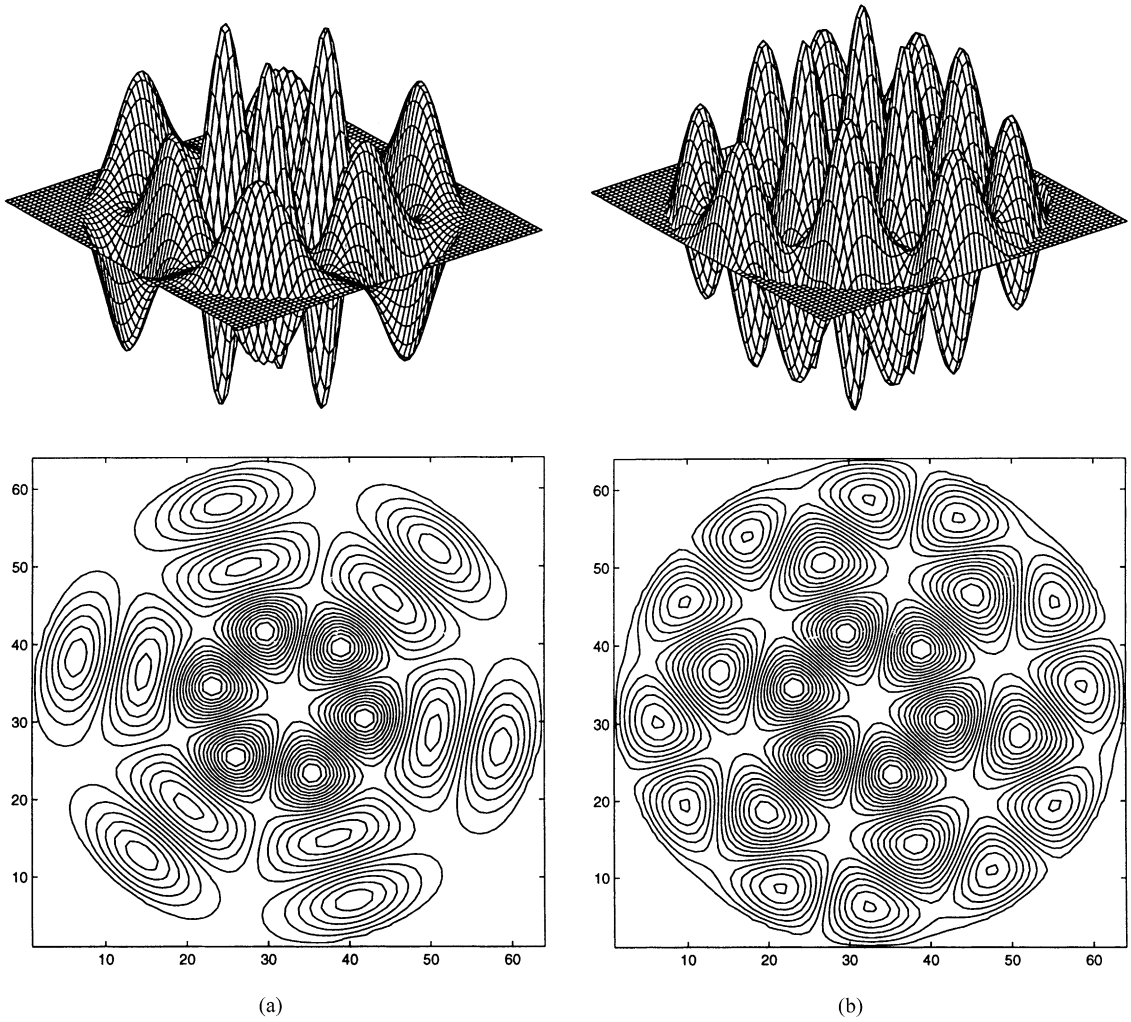

Fig. 4. (a)–(c) Mesh and contour plots of three typical patterns observed at $R = 12$ and the corresponding principal Fourier–Bessel mode: (a) $t = 800$; (b) $t = 830$; (c) $t = 840$; (d) pure Fourier–Bessel mode [3, 3].

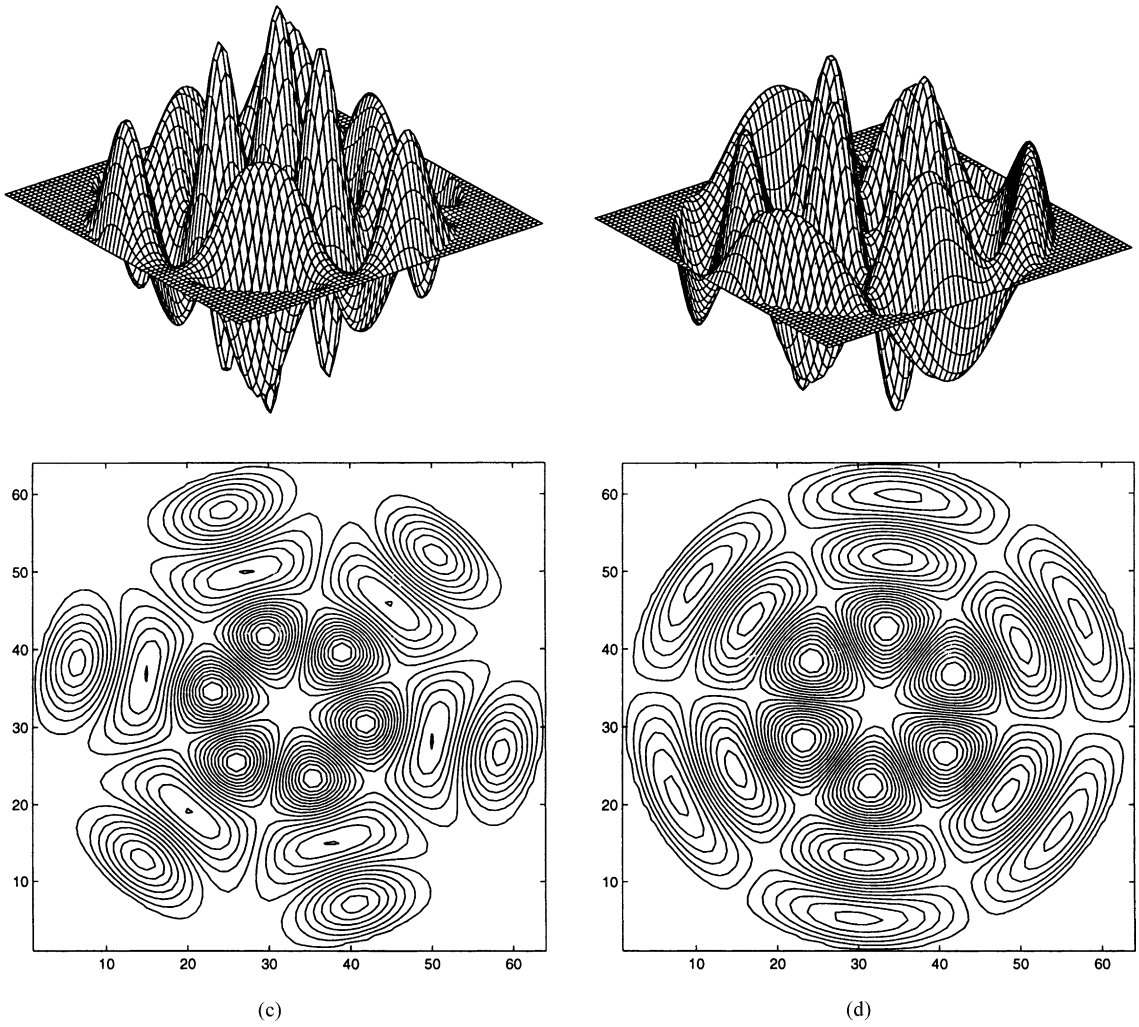

(c) (d)

Fig. 4. (*Continued*).

root value ($\rho_{n,m}$) of the Bessel function. A comparison of control parameter R used for obtaining these patterns and theoretical values $\rho_{n,m}$ for corresponding principal Fourier–Bessel modes $[n, m]$ are listed in Table 2. Generally, theoretical predictions match the experimental results very well. However, the discrepancy cannot be avoided due to the nonlinear nature of the Cahn–Hilliard equation and the Dirichlet boundary condition. The order of appearance of the patterns with increase in R is consistent with the well-known interlacing property of the Bessel functions' roots [19]:

$$0 < \rho_{1,m} < \rho_{1,m+1} < \rho_{2,m} < \rho_{2,m+1} < \rho_{3,m} \cdots .$$

Moreover, for a given m value, when R is large, it approximately takes a π increment in R to obtain the pattern with one more ring of cells, i.e., the value of n increases 1.

The question arises as to what happens if the control parameter R is simultaneously close to two or more roots of the Bessel function. In such a case, the

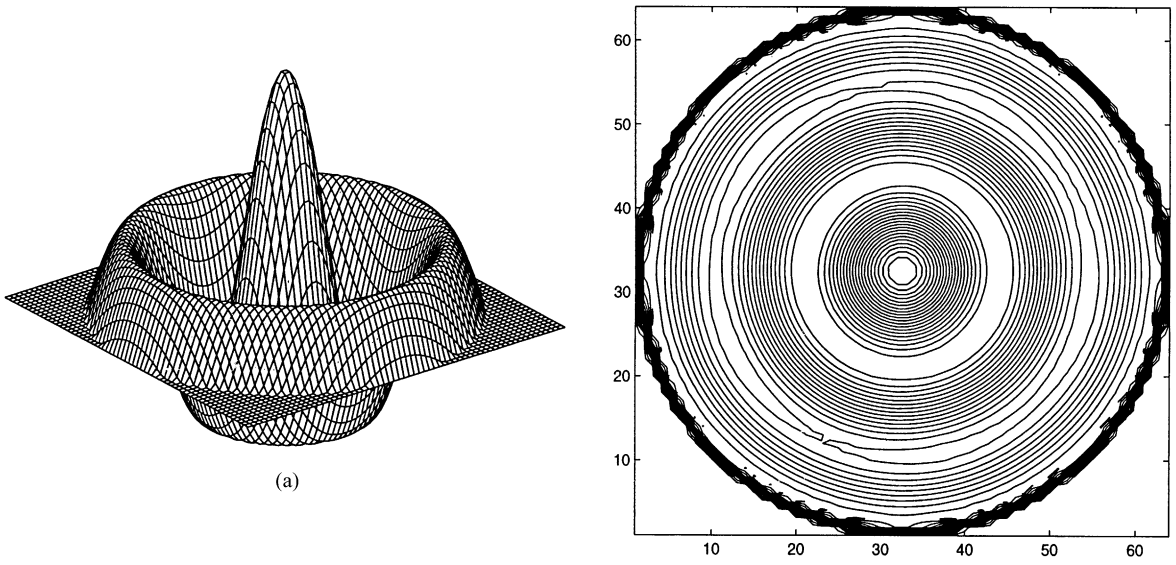

(a) (b)

Fig. 5. (a) Pure Fourier–Bessel mode [3, 0]; (b) contour plot for the difference between the computed pattern shown in Fig. 1(p) and pure Fourier–Bessel mode [3, 0].

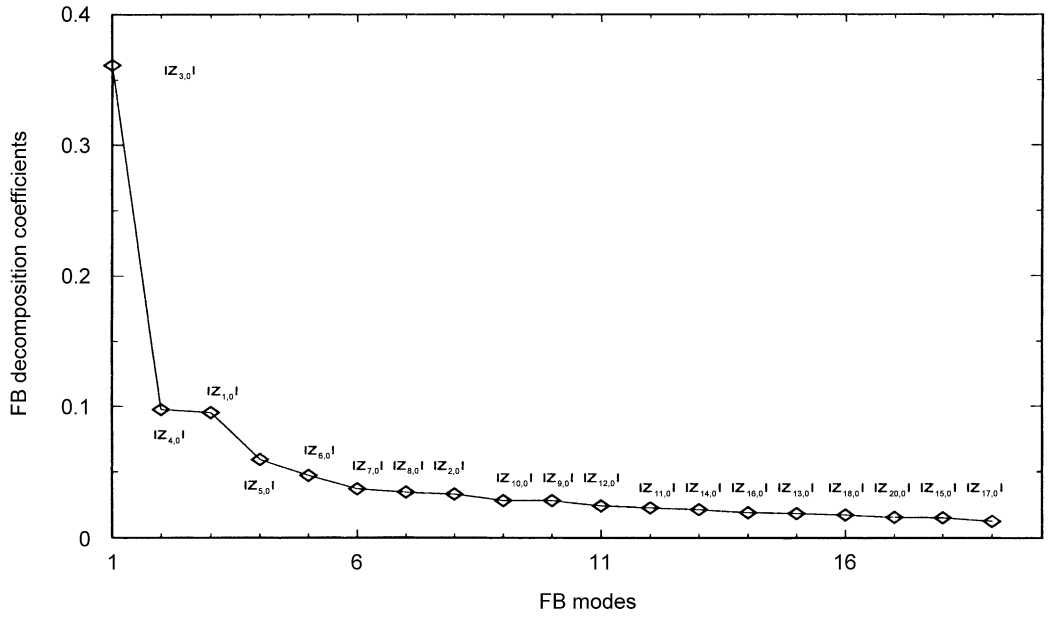

Fig. 6. Fourier–Bessel decomposition of the pattern shown in Fig. 1(p). The 19 largest Fourier–Bessel decomposition amplitudes which are greater than 0.01 are plotted by the decreasing order.

Table 2
A comparison of control parameters R used for attaining stable patterns and the corresponding non-trivial roots, $\rho_{n,m}$ of the Bessel function

m	$n=1$		$n=2$		$n=3$		$n=4$	
	R	$\rho_{1,m}$	R	$\rho_{2,m}$	R	$\rho_{3,m}$	R	$\rho_{4,m}$
0	–	–	5.5	5.520	8.25	8.654	11.0	11.792
1	4.0	3.832	6.5	7.016	9.75	10.173	–	–
2	5.0	5.136	8.0	8.417	10.875	11.620	–	–
3	6.0	6.380	9.25	9.761	12.0	13.015	–	–
4	7.5	7.588	10.5	11.065	–	–	–	–
5	8.5	8.771	11.5	12.339	–	–	–	–
6	9.375	9.936	12.5	13.589	–	–	–	–
7	10.0	11.086	–	–	–	–	–	–
8	11.375	12.225	–	–	–	–	–	–

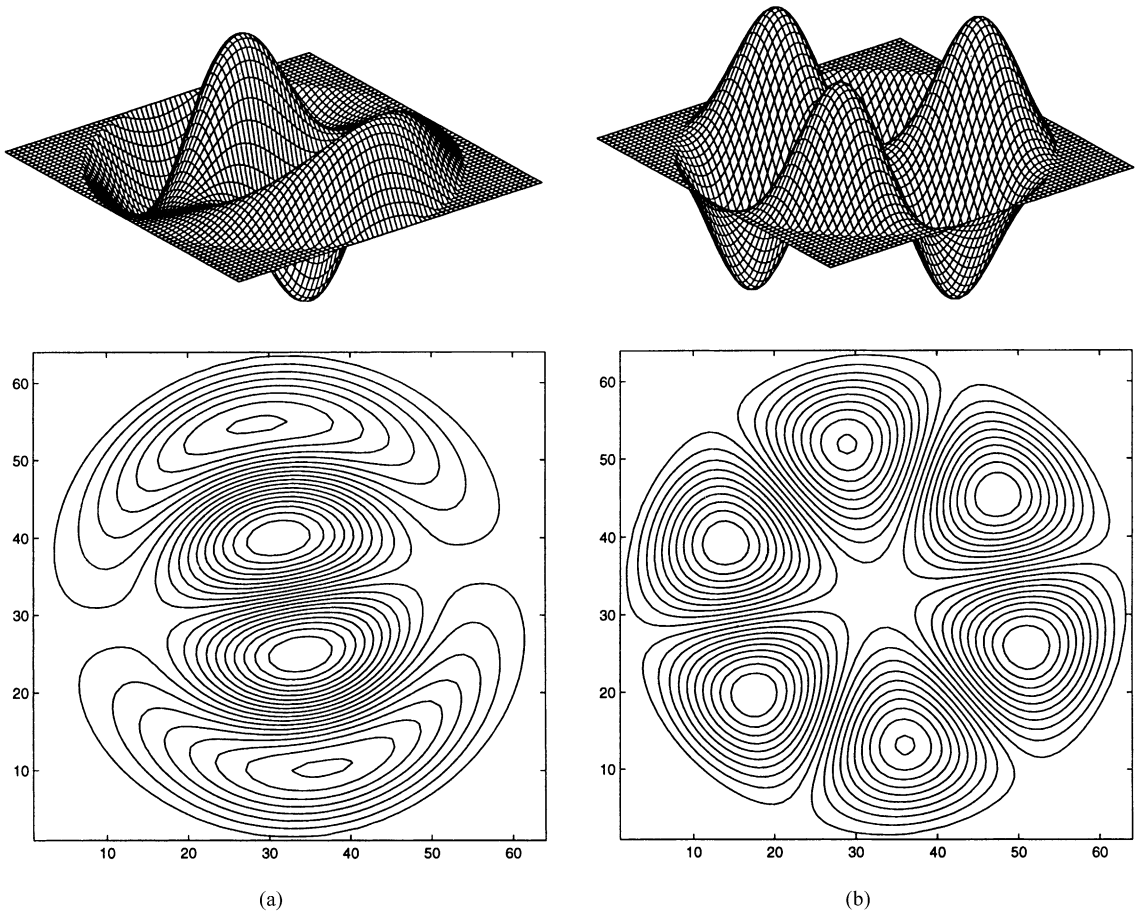

(a) (b)

Fig. 7. Mesh and contour plots of two typical patterns at $R = 6.5$: (a) $t = 920$; (b) $t = 1000$.

formation of patterns might be complicated by possible competition among different Fourier–Bessel modes since the system can stabilize itself at either principal Fourier–Bessel mode $[n, m]$ or $[n', m']$. Thus numerically it is possible to observe two or more different patterns at a given control parameter.

We illustrate a typical case in Fig. 7 — two observed patterns attained at a single control parameter. Fig. 7(a) plots a pattern having principal Fourier–Bessel mode $[2, 1]$ and Fig. 7(b) plots a pattern having principal Fourier–Bessel mode $[1, 3]$. Their corresponding Bessel roots are $\rho_{2,1} = 7.016$, and $\rho_{1,3} = 6.380$, respectively. Both roots are very close to the control parameter used, $R = 6.5$. Two corresponding principal Fourier–Bessel modes $[2, 1]$ and $[1, 3]$, compete to dominate the pattern morphology during the numerical integration with $R = 6.5$. Many similar cases are observed. For example, at $R = 10$,

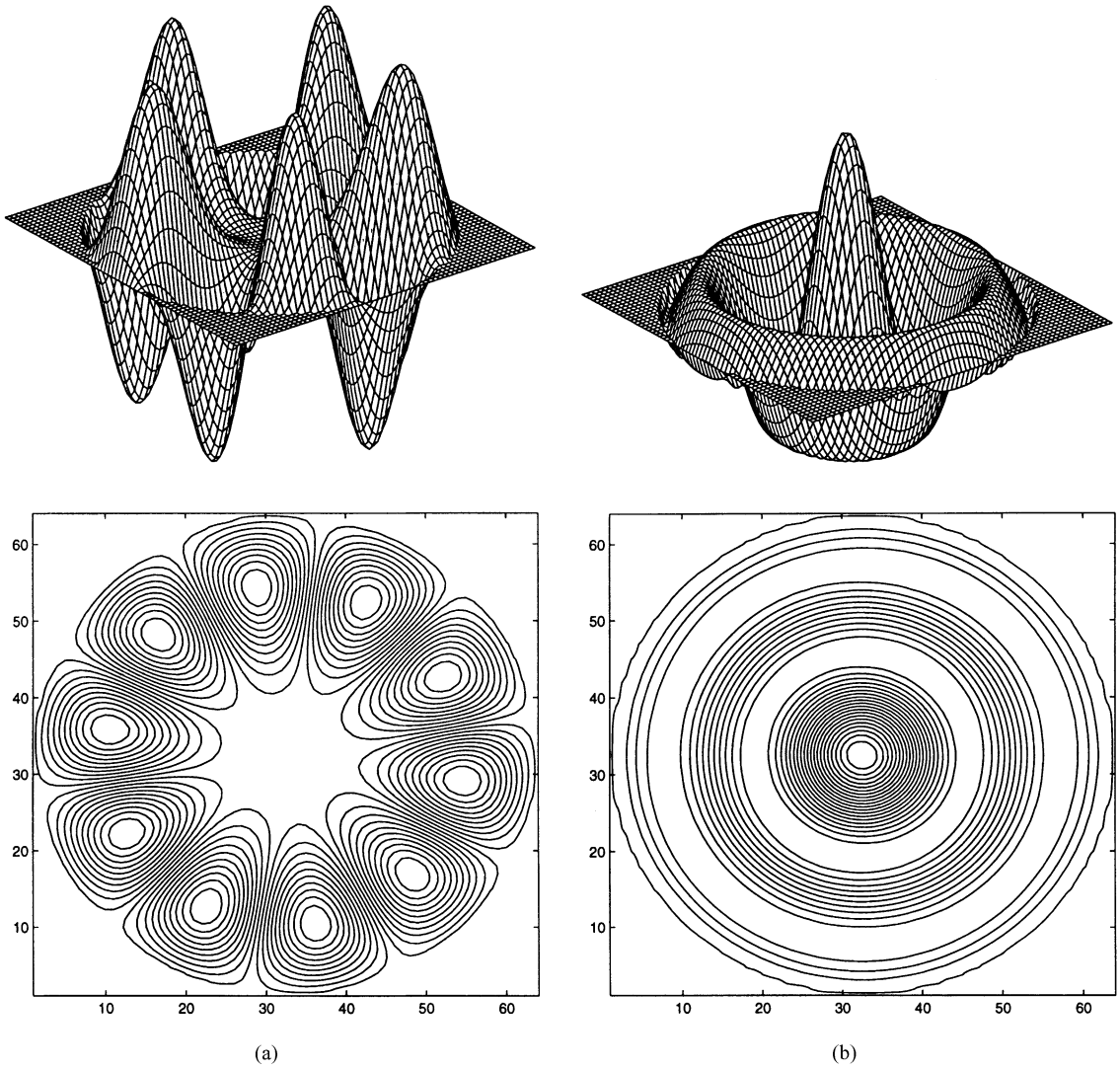

Fig. 8. (a)–(c) Mesh and contour plots of three typical patterns at $R = 8.25$: (a) $t = 310$; (b) $t = 380$; (c) $t = 870$; (d) a reconstructed pattern which corresponds to the transient pattern (c).

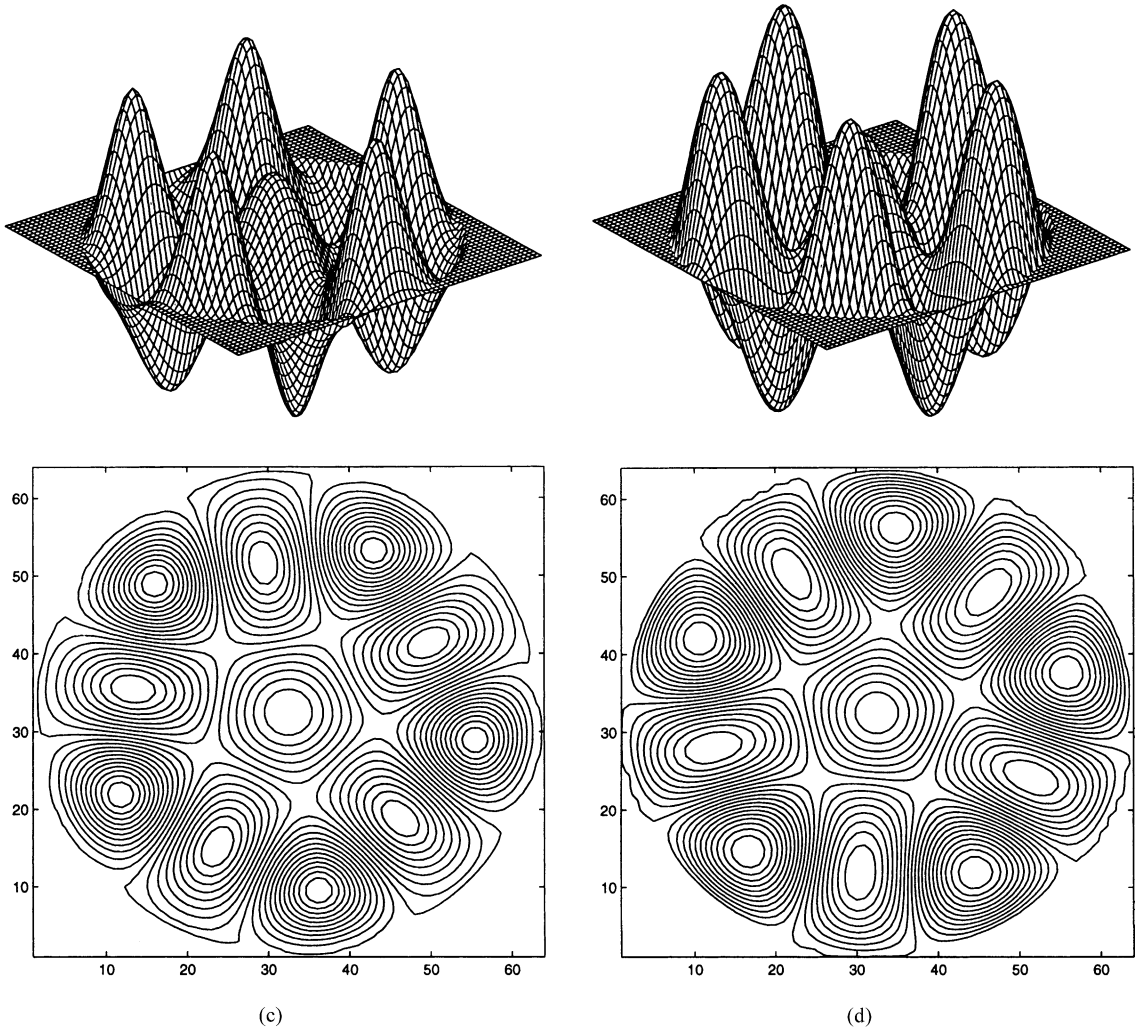

Fig. 8. (*Continued*).

three competing principal Fourier–Bessel modes are $[1, 7](\rho_{1,7} = 11.086)$, $[2, 4](\rho_{2,4} = 11.065)$ and $[3, 1](\rho_{3,1} = 10.173)$. Nevertheless, in all cases, the values of the control parameter R are qualitatively consistent with the theoretical roots of the Bessel functions. The intermediate patterns between two stable patterns are usually very irregular as the result of bifurcation and spontaneous multi-mode excitation. In addition, when n is sufficiently large, the density of Fourier–Bessel modes (number of modes per unit length of r) is also very large. In that case, multi-mode competition can be expected to occur frequently.

Fig. 8 illustrates another interesting case. The control parameter $R = 8.25$ is used for the numerical integration. Two resulting principal competing modes are $[1, 5]$ and $[3, 0]$ and their corresponding roots of the Bessel function are $\rho_{1,5} = 8.771$ and $\rho_{3,0} = 8.654$, respectively. The computed patterns are depicted in Fig. 8(a) and (b) for a comparison. The morphology of the patterns is dominated alternatively at different time steps by either principal Fourier–Bessel mode $[1, 5]$ or

[3, 0]. Modal decomposition of the pattern shown in Fig. 8(a) gives that $|Z_{1,5}| = 0.857$ and $|Z_{3,0}| = 0.014$. Obviously, Fourier–Bessel mode [3, 0] contributes little to this pattern. On the contrary, in the pattern shown in Fig. 8(b), the contribution of Fourier–Bessel mode [3, 0]($|Z_{3,0}| = 0.357$) is essential while the contribution of Fourier–Bessel mode [1, 5] is negligible ($|Z_{1,5}| = 0.000528$). However, this example is very different from the previous two cases. In the transient period, there is a stable pattern, Fig. 8(c), which is really a mixture of both Fourier–Bessel modes [1, 5] and [3, 0], with decomposition amplitudes $|Z_{1,5}| = 0.565$ and $|Z_{3,0}| = 0.141$, respectively. Because these two amplitudes are comparable, the two corresponding principal Fourier–Bessel modes contribute together to determine the morphology of the pattern in Fig. 8(c). A reconstructed pattern is depicted in Fig. 8(d), which is given by the linear combination ($c_1\Phi_{1,5} + c_2\Phi_{3,0}$, where $c_1 = 0.565$ and $c_2 = 0.141$) of the two pure Fourier–Bessel modes [1, 5] and [3, 0]. It is interesting to see that Fig. 8(c) and (d) are almost identical to each other.

Our computations are limited to the control parameter $R < 13$. Four complete classes ($n = 1$–4) of stable patterns are observed. The principal Fourier–Bessel mode [1, 0] is absent because it does not satisfy the conservation of order parameter. Obviously, as the control parameter R continues to increase, other series of stable state patterns ($n \geq 5$) can also be expected appear. However, further increase in R requires a more refined computational grid, which is more expensive in terms of computer resources.

4. Conclusion

In this study, the Fourier–Bessel analysis is utilized to characterize a new class of patterns generated from long-time integration of the phenomenological Cahn–Hilliard equation on a circular domain. It is found that generally all stable patterns can be expressed as a linear combination of Fourier–Bessel functions and they can be well classified by principal Fourier–Bessel modes. The morphologies of the patterns are mainly determined by the principal Fourier–Bessel modes, while non-principal Fourier–Bessel modes can slightly modify the shape of single-phase cells. In addition, modal competition among two or more Fourier–Bessel modes occurs when their corresponding roots of the Bessel function are close to a given control parameter value. In this case, the morphology of patterns can be dominated by anyone of the competing Fourier–Bessel modes. It is believed that our analysis is useful for the understanding of pattern formation of binary systems in a circular domain.

Acknowledgements

This work was supported by the National University of Singapore.

References

[1] V. Percec, C.-H. Ahn, G. Ungar, D.J.P. Yeardley, M. Möller, S.S. Sheiko, Controlling polymer shape through the self-assembly of dendritic side-groups, Nature 391 (1998) 161–164.
[2] N. Koneripalli, N. Singh, R. Levicky, F.S. Bates, P.D. Gallagher, S.K. Satija, Confined block copolymer thin films, Macromoleculars 28 (1995) 2897–2904.
[3] C. Bowman, A.C. Newell, Natural patterns and wavelets, Rev. Mod. Phys. 70 (1998) 289–301.
[4] M.C. Cross, P.C. Hohenberg, Pattern formation outside of equilibrium, Rev. Mod. Phys. 65 (1993) 851–1112.
[5] H. Furukawa, in: K. Kawasaki, M. Suzuki (Eds.), Formation, Dynamics, and Statistics of Patterns, Vol. 2, World Scientific, Singapore, 1993, pp. 266–308.
[6] J.W. Cahn, J.E. Hilliard, Free energy of a non-uniform system. I. Interfacial free energy, J. Chem. Phys. 28 (1958) 258–267.
[7] Y. Kuramoto, T. Tsuzuki, Persistent propagation of concentration waves in dissipative media far from thermal equilibrium, Prog. Theoret. Phys. 55 (1976) 356–369.
[8] J.D. Gunton, M.S. Miguel, P.S. Sahni, The dynamics of first-order phase transitions, in: C. Domb, J.L. Lebowitz (Eds.), Phase Transitions and Critical Phenomena, Vol. 8, Academic Press, London, 1983, pp. 267–482.
[9] S.G. Guan, C.-H. Lai, G.W. Wei, unpublished.
[10] G.W. Wei, Discrete singular convolution for the solution of the Fokker–Planck equations, J. Chem. Phys. 110 (1999) 8930–8942.
[11] Y. Meyer, Wavelets and Operators, Cambridge Studies in Advanced Mathematics, Vol. 37, Cambridge University Press, Cambridge, 1992.
[12] I. Daubechies, Orthonormal bases of compactly supported wavelets, Commun. Pure Appl. Math. 41 (1988) 909–996.

[13] I. Daubechies, Ten Lectures on Wavelets, CBMS-NSF Series in Applied Mathematics, SIAM, Philadelphia, PA, 1992.
[14] S. Mallat, Multiresolution approximations and wavelet orthonormal bases of $L^2(R)$, Trans. Am. Math. Soc. 315 (1989) 68–87.
[15] C.K. Chui, An Introduction to Wavelets, Academic Press, San Diego, CA, 1992.
[16] G.W. Wei, Quasi-wavelets and quasi-interpolating wavelets, Chem. Phys. Lett. 296 (1998) 215–222.
[17] G.W. Wei, Discrete singular convolution for the sine-Gordon equation, Physica D 137 (2000) 247–259.
[18] S. Rosenblat, S.H. Davis, G.M. Homsy, Nonlinear Marangoni convection in bounded layers. Part 1. Circular cylindrical containers, J. Fluid Mech. 120 (1982) 91–122.
[19] G.N. Watson, Theory of Bessel Functions, Cambridge Univ. Press, Cambridge, 1966.
[20] J.W. Cahn, J.E. Hilliard, Spinodal decomposition — a reprise, Acta Metall. 19 (1971) 151–161.